



PAPER

[View Article Online](#)
[View Journal](#) | [View Issue](#)Cite this: *Mater. Adv.*, 2025,
6, 1307

Enhancing the luminescence intensity of Eu^{3+} -activated $\text{NaYb}(\text{MoO}_4)_2$ phosphors through bismuth doping: Judd–Ofelt analysis, lighting, and temperature-sensing applications†

Yosra Bahrouni,^a Ikhlas Kachou,^a Kamel Saidi,^a  Tarak Kallel,^a
Mohamed Dammak,^a  ^{*} Irene Mediavilla^b and Juan Jiménez^b

In this work, we investigate the impact of Bi^{3+} doping on the luminescence properties of Eu^{3+} -activated $\text{NaYb}(\text{MoO}_4)_2$ phosphors synthesized via the conventional solid-state reaction method. Rietveld refinement of X-ray diffraction data confirmed the tetragonal crystal structure (space group $I4_1/a$) for all samples. UV-visible absorption spectroscopy revealed an indirect bandgap of approximately 3.25 eV for the 5% Bi^{3+} -doped sample. Under UV excitation, intense red emissions originating from the $^5\text{D}_0 \rightarrow ^7\text{F}$ transitions of Eu^{3+} ions were observed at 589 nm, 613 nm, 652 nm, and 700 nm, along with near-infrared emission from Yb^{3+} at 997 nm, sensitized by the MoO_4^{2-} group. Photoluminescence (PL) analysis demonstrated an enhancement in the Eu^{3+} emission intensity with increasing Bi^{3+} concentration, reaching an optimum at 5% Bi^{3+} doping. Chromaticity coordinates confirmed a significant enhancement in the red emission intensity upon Bi^{3+} incorporation. Judd–Ofelt parameters and crystal field parameters were determined, revealing that Bi^{3+} doping influences the local environment of Eu^{3+} ions, impacting the luminescence properties. Furthermore, we explored the potential of $\text{Bi}^{3+}/\text{Eu}^{3+}$ codoped $\text{NaYb}(\text{MoO}_4)_2$ for optical thermometry based on the fluorescence intensity ratio (FIR) technique, achieving a high relative sensitivity ($S_r = 1.14\% \text{ K}^{-1}$). This work demonstrates the influence of Bi^{3+} doping on the luminescence properties of Eu^{3+} in $\text{NaYb}(\text{MoO}_4)_2$ and explores its potential for applications in temperature sensing and other optoelectronic devices.

Received 26th November 2024,
Accepted 8th January 2025

DOI: 10.1039/d4ma01167h

rsc.li/materials-advances

Introduction

The field of luminescence thermometry is experiencing intense growth, with significant advances in detection, imaging, diagnostics, and therapy, among others. This interest has been stimulated mainly by the fact that many of today's technological requirements in fields such as micro- and nanoelectronics, photonics, nanomedicine, micro- and nanofluidics¹ have reached a point where the use of traditional contact thermal probes is unable to provide reliable measurements when the spatial resolution enters the submicron range. This limitation of conventional thermometers for small systems has stimulated the development of luminescent micro- and nano-thermometers.² Moreover, from an industrial point of view, this expected

miniaturization should make it possible to bring new nanoscale thermal probes to the market. Although the recently developed luminescent nanothermometers are radically more sophisticated and involve complex synthesis procedures, the fundamental problems and applications addressed are similar to those reported at the beginning of the field: understanding heat and energy transfer mechanisms, optimizing temperature readout, and developing efficient cost-effective sensors for advanced medical and engineering tools. Among the various emitting centers used in luminescence thermometry, one can include proteins, nucleic acids and other biomolecules, thermosensitive polymers,^{3,4} organic dyes and QDs.⁵ Systems include molecular complexes, MOFs, organic–inorganic polymers and hybrids, multifunctional thermometer nanoplateforms, and UC, DC, and DS materials. This article describes the use of Ln^{3+} lanthanide and transition-metal ion co-doped phosphors as luminescent ratiometric thermometers aiming for the use of luminescence thermometry for thermal imaging.⁶ Lanthanide ions (Ln^{3+}) (such as Eu^{3+} , Tb^{3+} , Dy^{3+} , and Sm^{3+}) are used as the reference signals, while transition-metal ions (such as Mn^{4+} and Bi^{3+}) are chosen for detection signals due to their different thermal quenching

^a Laboratoire de Physique Appliquée, Faculté des Sciences de Sfax, Département de Physique, Université de Sfax, BP 1171 Sfax, Tunisia.E-mail: madidammak@yahoo.fr, mohamed.dammak@fss.usf.tn^b GdS Optronlab, Department of Condensed Matter Physics, LUCIA Building, University of Valladolid, Paseo de Belén 19, 47011, Valladolid, Spain† Electronic supplementary information (ESI) available. See DOI: <https://doi.org/10.1039/d4ma01167h>

mechanisms^{7–10} for early tumor detection, but also as a tool to unveil the properties of the thermometers themselves or their local environment.¹¹ Numerous applications in lighting devices have been found when doped with rare-earths.¹² The Eu^{3+} ion, which generally exhibits intense red fluorescence corresponding to the $^5\text{D}_0 \rightarrow ^7\text{F}_2$ emission transition at around 620 nm, is often used as the active center in red phosphors in many industrial applications. Spectroscopy of the Eu^{3+} ion is also of particular interest because of its extreme sensitivity to the crystalline environment, enabling it to be used as a point probe in many materials, especially those containing rare-earth cations whose ionic radii are close to that of Eu^{3+} .^{13–15} Bismuth is a non-rare-earth metal ion. It is considered the least toxic of the heavy metals, which has been the subject of intensive research in recent years due to its special optical characteristics.¹⁶

As a typical non-rare earth activator, Bi^{3+} emits light *via* the $^3\text{P}_1 \rightarrow ^1\text{S}_0$ transition.¹⁷ This emission is highly dependent on the crystal field environment and structural symmetries. Therefore, phosphors doped with Bi^{3+} can emit luminescence at different wavelengths, such as ultraviolet (UV), visible, and infrared light.¹⁸ It can also be used as a sensitizer in order to efficiently transfer the absorbed NUV or UV energy to Eu^{3+} or Sm^{3+} ions. Besides, the selection of appropriate host materials is important as the host has a significant influence on the emission of the Ln^{3+} ions. Some of the hosts that have been used as a part of the Ln^{3+} doped red emitting phosphors are fluorides, germanates, vanadates, tungstates and molybdates.^{19,20} According to the existing literature, many reports have been devoted to synthesizing and characterizing the luminescence properties of lanthanide doped molybdate microcrystals or phosphors. Moreover, molybdates have been extensively studied for their remarkable properties such as high chemical stability, brilliance, high melting point, low chemical toxicity and long persistence without radioactive irradiation.^{21–23}

However, molybdate phosphors present several problems. For example, SrZnMoO_6 and $\text{NaY}(\text{MoO}_4)_2$ phosphors have low efficiencies of self-activating emission, which is not suitable for solid-state lighting.²⁴ In addition, some molybdate phosphors such as $\text{NaY}(\text{MoO}_4)_2:\text{Eu}^{3+}$ have low energy transfer (ET) efficiency from MoO_4^{2-} groups to rare earth ions,²⁵ therefore, tunable luminescence is difficult to achieve. In contrast to these MoO_4^{2-} weaknesses, SrZnMoO_6 vanadate presents high luminescence efficiency and a high ET efficiency. Many reports show that codoping with Bi^{3+} permits to enhance the luminescence performance of phosphors, such as $\text{CaMoO}_4:\text{Bi}^{3+}/\text{Eu}^{3+}$, $\text{CaY}_4(\text{SiO}_4)_3\text{O}:\text{Bi}^{3+}/\text{Eu}^{3+}$ and $\text{BaLa}_2\text{Si}_3\text{O}_{10}:\text{Eu}^{3+}/\text{Bi}^{3+}$ phosphors,^{26,27} because of the sensitizer role of Bi^{3+} ions. While this progress is promising, a need remains for materials with improved thermal stability, improved luminescence, and precise temperature sensitivity for a broader range of applications.

Many research groups are constantly searching for new ratio-metric thermometers with improved thermometric performance. Conventional FIR analysis requires expensive equipment, time-consuming measurements followed by complicated data processing, and considering a variety of rare earth ions and potential hosts. However, it is difficult to control all these materials from a thermometric point of view using a traditional approach. In order

to solve this problem, Ciric *et al.* developed an extension of the Judd–Ofelt theory to the field of lanthanide thermometry, which allows calculation of the thermometric performances from the single emission spectrum measured at room temperature.²⁸ The theoretically calculated parameters may differ slightly from those obtained experimentally due to imperfections in the Judd–Ofelt theory and in the acquisition and treatment of spectroscopic data. However, Ciric *et al.* demonstrated the applicability of the model for the difficult case of Eu^{3+} doped Y_2O_3 samples, which have the largest discrepancy between theoretical and experimental parameters due to the largest energy gap among rare earth ions.¹⁵

We aim here to investigate the effects of Bi^{3+} on the structural, optical and thermometric properties of Bi^{3+} -codoped Eu^{3+} -activated $\text{NaYb}(\text{MoO}_4)_2$ (NYMO) phosphors, in order to optimize its performance for optoelectronic and temperature sensing applications.

Experimental section

Materials and preparation

A series of NYMO compounds doped with Eu^{3+} and codoped with Bi^{3+} ($\text{NYMO}:0.05\text{Eu}^{3+}/y\text{Bi}^{3+}$, where $y = 0, 0.05, 0.15, 0.2$) were successfully synthesized *via* a solid-state reaction. The precursors Na_2CO_3 , MoO_3 , Bi_2O_3 , Y_2O_3 , and Eu_2O_3 were weighed in stoichiometric ratios and thoroughly mixed in an agate mortar for 15 minutes. The resulting mixture was dried in a furnace at 350 °C. After regrinding for 1 hour, the precursor powder was placed in alumina crucibles and sintered at 600 °C for 12 hours in an air atmosphere. Then, they undergo post-calcination under an oxygen flow to ensure appropriate oxygen stoichiometry. The annealing duration was sufficient for grain formation and growth, ensuring the structural integrity of the final product.

Characterization

X-ray diffraction radiation (XRD) was used to check the crystal-line structure and phase purity of the samples. The morphology and microstructures of the phosphors were analyzed by scanning electron microscopy (SEM) images which were photographed on a Hitachi SU-4800 field-emission SEM. UV-Vis-NIR absorption measurements are carried out with a UV-Vis-NIR spectrometer (PerkinElmer Lambda 950). Added to this, the photoluminescence excitation (PLE) and photoluminescence (PL) spectra as a function of temperature were recorded by using a Fluoromax-4P fluorometer (HORIBA) spectrophotometer.

Results and discussion

Structural study and morphology

The synthesized particles were subjected to extensive analysis to confirm their composition and morphology. The structure and phase purity of the $\text{NYMO}:0.05\text{Eu}^{3+}/y\text{Bi}^{3+}$ ($y = 0, 0.05, 0.15$ and 0.2) were determined by XRD analysis (Fig. 1). The particles exhibited high crystallinity and an ordered tetragonal phase, according to the $\text{NaYb}(\text{MoO}_4)_2$ reference model in JCPDS No. 04005-9926.²⁹ Furthermore, the crystal structure of the



resulting samples using Rietveld structure refinements of NYMO:0.05Eu³⁺ with different Bi³⁺ fractions ($y = 0, 0.05, 0.15$ and 0.2), was obtained, Fig. S1 (ESI†). The Yb³⁺ and Mo⁶⁺ ions are coordinated with six and four oxygen atoms respectively. The Yb³⁺ radius is 0.0985 nm (0.985 Å, CN = 8), the Bi³⁺ radius is 0.117 nm (1.17 Å, CN = 8), and the Eu³⁺ radius is 0.1066 nm (1.066 Å, CN = 8).³⁰ Additionally, the crystallographic structure of the NYMO unit cell along with the coordination geometry of oxygen ions surrounding the Yb³⁺, Eu³⁺ and Bi³⁺ ions is drawn and presented in Fig. 1. The refined lattice parameters, cell volume as well as structural parameters are given in Table S1 (ESI†). However, as indicated in Table S2 (ESI†), the length of the Mo → O²⁻ bond changes slightly with the increase of Bi³⁺.³¹ Meanwhile, the percentage differences between the dopants and the substituted ions are obtained using the following equation:³²

$$D_r = \frac{R_s - R_d}{R_s} \times 100\% \quad (1)$$

where D_r is the percentage difference in radius. R_s and R_d denote substituted ion and dopant ionic radii respectively. The dopants (Eu³⁺ and Bi³⁺) are expected to occupy the sites of the Yb³⁺ ions in the NYMO host lattice, given the effective ionic radii and the charge balance of the cations. Using eqn (1), the D_r values of Yb³⁺/Eu³⁺ and Yb³⁺/Bi³⁺ were estimated to be $\approx 7.59\%$ and 15.81% , respectively. These calculated D_r values indicate that Eu³⁺ and Bi³⁺ ions can easily enter into the NYMO host lattice by substituting Yb³⁺ ions, as the D_r values are much smaller than 30%. It is worth noting that the cell volume increases when the small-radius ions are replaced by the large-radius ions. According to the results of the refinements, the cell volume gradually increases with the doping with Bi³⁺ ions. This is mainly due to the greater electronegativity of Bi³⁺ ions with respect to the Yb³⁺ ions. When Bi³⁺ ions are incorporated, the average bond length becomes larger, resulting in both the increase of the interplanar space and the cell volume. As the bond length changes a concomitant distortion of the lattice takes place inducing strain. The degree of distortion can be determined using the following expression:³³

$$D(\text{TO}) = \frac{(\sum |\text{TO}_i - \text{TO}_m|)}{6\text{TO}_m} \quad (2)$$

where TO_i is the individual cation to ligand anion distances, and TO_m is the average bond length.

The results are illustrated in Fig. S2 (ESI†). The distortion of the samples decreases with the Bi³⁺ doping concentration, which can lead to the crystal field splitting. Furthermore, the lattice distortion is inversely proportional to the variation of the volume.

The morphology of the samples doped with Eu³⁺ and codoped Eu³⁺/Bi³⁺ in NYMO phosphors was observed by SEM. Fig. 2 illustrates the SEM images of NYMO:0.05Eu³⁺ (a), and NYMO:0.05Eu³⁺/0.05Bi³⁺ (b). Moreover, it can be concluded from the SEM images that the grain conglomeration is not obvious. The particle sizes in sample NYMO:0.05Eu³⁺/0.05Bi³⁺ are smaller than those shown in Fig. 2(a), with both being well below 10 μm .

Optical characterization

UV-Visible. The diffuse reflectance spectra of the NYMO:5% Eu³⁺/yBi³⁺ samples are depicted in Fig. S3 (ESI†), revealing interesting features that reflect the chemical composition and optical properties of these materials. The absorption peaks characteristic of Yb³⁺ ion transition from the ground state $^2F_{7/2}$ to the excited state $^2F_{5/2}$, along with the f-f transitions of the Eu³⁺ ion, are observed in the infrared and visible regions, respectively, indicating the effective presence of these dopant ions. These peaks are accompanied by a broad absorption band in the near-ultraviolet region, attributed to the $6s^2 \rightarrow 6p^1$ transition of bismuth (Bi³⁺). In addition, two distinct absorption bands in the blue and violet region are attributed to the ligand-to-metal (LMCT) and charge-transfer (CT) transitions of the MoO₄²⁻ group.

It is worth pointing out that another factor can influence the luminescence emission of lanthanide ions, particularly in systems doped with Eu³⁺. Due to its 4f⁶ electronic configuration, the Eu³⁺ ion must absorb an extra electron to reach the more stable 4f⁷ configuration. When Eu³⁺ is bound to O²⁻ ligands, electron transfer can occur from the 2p oxygen orbital to the 4f⁷ orbitals. Two intense bands peaking at 212 and 253 nm are assigned to the charge transfer band (CTB), which can then be transferred non-radiatively to energy levels

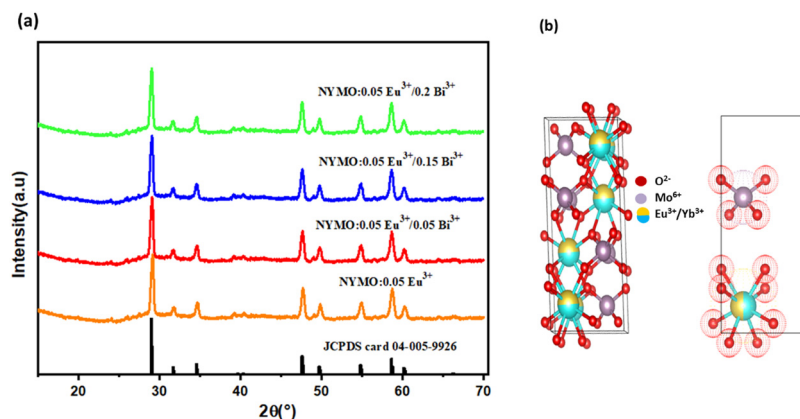


Fig. 1 (a) XRD powder patterns of NYMO:0.05Eu³⁺/yBi³⁺ samples. The standard data for NaYb(MoO₄)₂ (JCPDS card 04-005-9926) are also presented for comparison and (b) the view of the structure of NYMO:0.05Eu³⁺/0.05Bi³⁺.



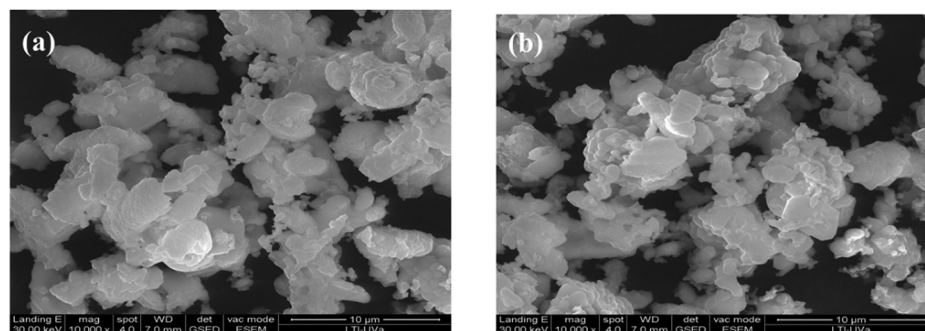


Fig. 2 SEM images of (a) NYMO:0.05Eu³⁺, and (b) NYMO:0.05Eu³⁺/0.05Bi³⁺.

associated with Eu³⁺. The corresponding band in the excitation spectrum is known as the Eu–O charge transfer band (CTB).³⁴ Furthermore, the band detected at 360 nm is attributed to the ¹S₀ → ¹P₁ Bi³⁺ transition.¹⁷ Doping with Bi³⁺ ions leads to the emergence of additional energy levels in the form of a continuous band. In addition, this doping process generates extra valence electrons from the 6s² state.¹⁸ One observes that the optical band gap increases with respect to the host, and it is estimated to vary from 3.02 eV to 3.25 eV when the concentration of Bi³⁺ ions increase from 0% up to 20%.

Photoluminescence properties

To examine the sensitizing effect of Bi³⁺ ions on NYMO:0.05Eu³⁺ samples, a series of NYMO samples co-doped with Bi³⁺ and Eu³⁺ ions were successfully synthesized. Fig. 3a illustrates the PL excitation spectra of the host NYMO monitored at 615 nm emission wavelength. The spectrum displays a broad band in the range of 285 to 350 nm and a sequence of sharp bands in the range of 350 to 500 nm. The broadband with a maximum at 330 nm is related to the charge transfer from O^{2−} → Eu³⁺, Mo⁶⁺ ions. There is a marked improvement in the charge transfer band when different concentrations of bismuth are added.^{35,36}

Moreover the sharp peaks located at 363 nm (⁷F₀ → ⁵L₇), 382 nm (⁷F₀ → ⁵D₄), 394 nm (⁷F₀ → ⁵L₆), 416 nm (⁷F₀ → ⁵D₃), 464 nm (⁷F₀ → ⁵D₂) and 535 nm (⁷F₀ → ⁵D₁) are attributed to the 4f–4f transitions of Eu³⁺ ions.^{37,38} Based on the excitation spectra, the two peaks centered at 464 and 535 nm exhibit stronger intensities, suggesting that NYMO:Eu³⁺ phosphors can be efficiently pumped by UV light. On the other hand, Fig. 3b shows the photoluminescence emission spectra of NYMO:0.05Eu³⁺/yBi³⁺ microcrystals under excitation with UV light at 325 nm from a He–Cd laser. Emission bands at 702 nm (⁵D₀ → ⁷F₄), 654 nm (⁵D₀ → ⁷F₃), 613 nm (⁵D₀ → ⁷F₂), 589 nm (⁵D₀ → ⁷F₁) and 533 nm (⁵D₁ → ⁷F₂) are associated with Eu³⁺ transitions.^{39,40} To understand these luminescence transitions, it is important to consider the crystal field splitting of the energy levels. The most intense transitions occur from the ⁵D₀ level onwards, which remains non-degenerate (*J* = 0) by the crystal field. According to Judd–Ofelt theory, transitions to even-numbered *J* levels are considerably more intense than those to their odd-numbered counterparts. Thus, the dominant red peak at around 614 nm is attributed to the hypersensitive ⁵D₀ → ⁷F₂ transition with Δ*J* = 2.^{41,42} Additionally, one emission peak at 993 nm is associated with transitions related to Yb³⁺.⁴³ No discernible peaks corresponding to the presence of Bi³⁺ ions were observed.²⁵ Moreover, the emission intensity is

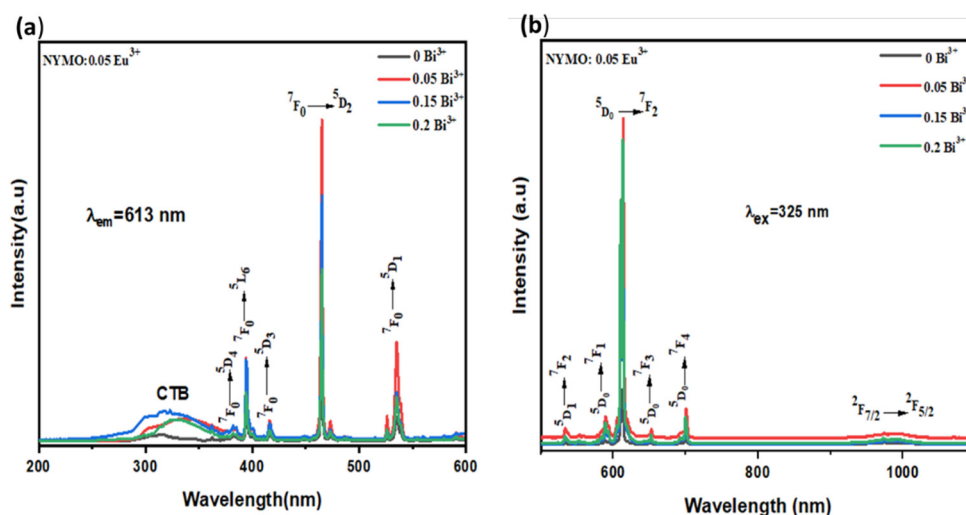


Fig. 3 Excitation and emission spectra of the NYMO:0.05Eu³⁺/yBi³⁺ phosphors monitored at λ_{em} = 615 nm, and λ_{ex} = 325 nm respectively.



gradually enhanced with the doping Bi^{3+} ions, which gives support to the successful incorporation of Bi^{3+} ions into the NYMO lattice. The Bi^{3+} ion concentration was $y = 0, 5, 15, 20\%$, and it appears that the optimal emission corresponds to $5\% \text{Bi}^{3+}$.

Photometric characterization (CIE)

Based on the detected PL emission spectra, the phosphor's emission color can be mathematically expressed using the Commission International de l'Eclairage (CIE) chromaticity coordinates,⁴⁴ and the CIE coordinates for $\text{Eu}^{3+}/y\text{Bi}^{3+}$ codoped $\text{NaYb}(\text{MoO}_4)_2$ phosphors were evaluated from the respective emission spectra monitored at 325 nm excitation. The CIE chromaticity diagram is illustrated in Fig. 4. The color coordinates of $\text{Eu}^{3+}/y\text{Bi}^{3+}$ codoped $\text{NaYb}(\text{MoO}_4)_2$ phosphors are summarized in Table S3 (ESI†). It is seen that the CIE coordinates are close to each other. They all fall within the red region. The phosphor exhibits excellent light-color conversion efficiency.

The correlated color temperature (CCT), which characterizes the color appearance of the light emitted by a light source, is another essential measure for evaluating the overall emission of phosphors. The CCT value of the phosphor can be determined from the CIE color coordinates (x, y) using the McCamy relationship.⁴⁵

It should be noted that phosphors with CCT values above 4000 K are generally considered to be cold light sources, while those with CCT values below 3200 K are regarded as warm light sources in appearance.⁴⁶ NYMO phosphors doped with $0.05\text{Eu}^{3+}/y\text{Bi}^{3+}$ have CCT ranging from 1977 to 2262 K. The CCT values obtained are all below 3200 K, indicating that the NYMO: $\text{Eu}^{3+}/y\text{Bi}^{3+}$ phosphors fall within the warm light category.

The color purity of the phosphors is crucial for enhancing light sources in LED applications. The concept is particularly beneficial for light sources that emit light within a narrow range of wavelengths. For light sources that emit in a wide range of wavelengths (such as white light), the CCT is more advantageous. Therefore, it is essential to determine the color purity of the emitted red light.⁴⁷

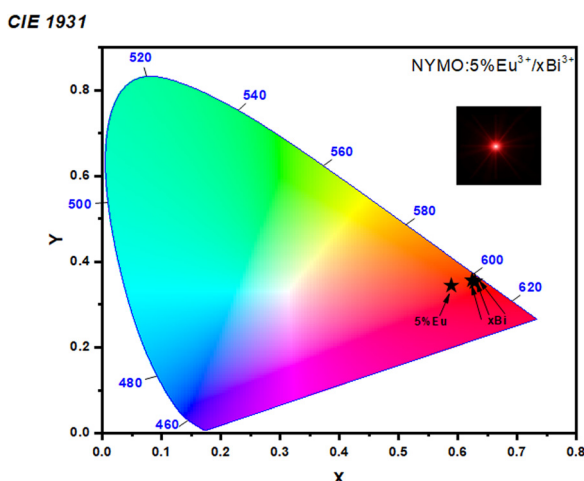


Fig. 4 CIE 1931 chromaticity diagram of NYMO phosphors codoped with $0.05\text{Eu}^{3+}/y\text{Bi}^{3+}$ excited at $\lambda_{\text{ex}} = 325 \text{ nm}$.

The calculated CCT values for all as-synthesized samples range from 1977 K to 2262 K as illustrated in Table S3 (ESI†). Furthermore, the addition of different concentrations of Bi^{3+} leads to an improvement in both color purity and CCT values. A pronounced red shift is thus observed. The purity of the color peaks is 87.21% for a Bi^{3+} concentration of 5%. The results of the chromaticity study confirm that the NYMO: $\text{Eu}^{3+}/y\text{Bi}^{3+}$ compound has significant potential application in white LEDs as a red-emitting phosphor.

Judd–Ofelt analysis

To further investigate the local environment around the Eu^{3+} ions in the NYMO host, the Judd–Ofelt (JO) analysis is a practical tool for understanding the detailed site symmetry and luminescence of rare earth ions in a specific coordination environment. Judd–Ofelt parameters are generally derived from absorption spectra, but can be determined from emission spectra for the Eu^{3+} ion, as it has a simple energy diagram.⁴⁷

In this study, it was possible to calculate the parameters $J-O$, Ω_2 and Ω_4 from the emission spectra because the Eu^{3+} ion has a special energy structure under 325 nm excitation. However, the intensity parameter Ω_6 was not determined because the $^5\text{D}_0 \rightarrow ^7\text{F}_6$ transition was not detected in the PL spectra.⁴⁸ Indeed, Ω_2 is strongly influenced by the environment in which Eu^{3+} ions are found. Thus, the maximum value of Ω_2 may be associated with variations in the environment structure of the Eu^{3+} ion due to its high sensitivity to the $^5\text{D}_0 \rightarrow ^7\text{F}_2$ transition.⁴⁹ A higher value of Ω_2 often indicates that the symmetry of sites containing Eu^{3+} ions is altered. As for Ω_4 ($^5\text{D}_0 \rightarrow ^7\text{F}_4$), it is linked to the strength and stability of the matrix surrounding the rare earth ions.⁴⁷ In this case, the JO parameters for Eu^{3+} -doped NYMO were calculated using JOES software.⁵⁰ The value of the refractive index used was reported in the literature ($n = 1.99$).⁵¹ The values obtained are listed in Table S4 (ESI†). For europium doping with different Bi^{3+} concentrations, the trend observed in the J–O parameters ($\Omega_2 > \Omega_4$) confirms that the bond is covalent.⁵² These theoretical calculations are in good agreement with the experimental results obtained from the XRD profile and photoluminescence spectra.

The analysis of J–O intensity parameters in NYMO phosphors co-doped with varying concentrations of Bi^{3+} provides insightful conclusions regarding the luminescent properties of the material. Table S4 (ESI†) summarizes the average J–O intensity parameters, specifically Ω_2 and Ω_4 , for different Bi^{3+} concentrations. As the Bi^{3+} concentration increases from 0 to 0.05, the Ω_2 parameter rises to $15.182 \times 10^{-20} \text{ cm}^2$, indicating enhanced electric-dipole transition probability associated with the Eu^{3+} ions. However, at higher concentrations (0.15 and 0.2Bi^{3+}), Ω_2 stabilizes around 14.729 and $14.858 \times 10^{-20} \text{ cm}^2$, respectively, suggesting that the positive influence of Bi^{3+} on the local symmetry and transition strength reaches saturation. Conversely, the Ω_4 parameter shows a decline from $4.186 \times 10^{-20} \text{ cm}^2$ at 0Bi^{3+} to $3.351 \times 10^{-20} \text{ cm}^2$ at 0.05Bi^{3+} , followed by a slight increase at 0.15Bi^{3+} ($3.515 \times 10^{-20} \text{ cm}^2$) and a subsequent decrease again at 0.2Bi^{3+} ($3.204 \times 10^{-20} \text{ cm}^2$). This trend indicates that the higher Bi^{3+} concentration may negatively



impact the parity of the transitions, reducing the associated transition probability for the transitions governed by Ω_4 .

These results suggest that a low concentration of Bi^{3+} ($y = 0.05$) optimizes the J–O parameters, enhancing the luminescence of the Eu^{3+} ions due to improved electric-dipole transitions. However, for further increase in Bi^{3+} concentration, the effectiveness diminishes, indicating the need for a careful optimization of Bi^{3+} doping in order to maximize the optical response of the phosphors for applications in optoelectronic devices.

Crystal-field calculation

The second-order crystal field (CF) parameters, B_{20} and B_{22} , characterize the interaction between the magnetic moment of the Eu^{3+} ion and the electric crystal field generated by its local environment. These parameters are key to understanding the spectroscopic and luminescent properties of lanthanide-doped materials.

In the present case, the CF parameters B_{20} and B_{22} have been calculated from the Stark levels of the $\text{Eu}^{3+} {}^7\text{F}_1$ ground level in the S_4 symmetry crystal structure.⁵³ This analysis provides precise information on the nature of the crystal field and its influence on the 4f orbitals of the Eu^{3+} ion.⁵⁴

In addition to parameters B_{20} and B_{22} , it is also important to calculate the parameter S_2 , which represents the strength of the spin–orbit interaction. This parameter is important for understanding the splitting of Eu^{3+} f–f energy levels due to the interaction between its spin and orbital moment, and we calculate the values of B_{20} , B_{22} and S_2 .⁵⁵ The evolution of the crystal field (CF) parameters B_{20} and B_{22} as a function of Bi^{3+} concentration highlights the influence of this dopant on the crystal structure and luminescent properties as shown in Fig. S4 and Table S5 (ESI†). Since our study focuses on the effect of bismuth, we carried out a comparison with other matrices, Table S6 (ESI†). These results imply that moderate Bi^{3+} doping (around 5–15%) enhances the crystal field strength, potentially optimizing its luminescence performance. However, high concentrations (20% Bi^{3+}) lead to a more substantial alteration in the crystal field, which seems to affect the luminescence mechanisms and thermometric sensitivity. The variation of these parameters highlights the critical role played by Bi^{3+} doping in modulating the crystal environment and optimizing the optical properties of the material.

From the above analysis, the value of B_{20} was estimated at 55 cm^{-1} and gradually decreases down to an optimal Bi concentration. This decrease suggests that the introduction of Bi^{3+} into the crystal structure modifies the local symmetry around the Eu^{3+} ion, resulting in a reduction in the CF interaction between the crystal field and the Eu^{3+} 4f orbitals. On the other hand, the value of B_{22} increases up to a concentration of 5% Bi^{3+} decreasing thereafter. This observation indicates that the effect of Bi^{3+} on the crystal field is more complex and depends on the dopant concentration. It is possible that the initial increase in B_{22} is linked to a Bi^{3+} -induced distortion of the crystal structure, while the subsequent decrease reflects a stabilization of the structure.

The overall analysis of the evolution of the CF parameters B_{20} and B_{22} suggests that the effect of Bi^{3+} on the luminescent properties of the material is linked to modification of CF around the Eu^{3+} ion. This modification may influence the relaxation processes of excited electrons and, consequently, the intensity and efficiency of the luminescence emission. In accordance with the structural results, which confirm that the addition of bismuth reduces the distortion modifying the structure. Therefore, the results obtained can be explained in terms of the distortion of the tetragonal structure, which lifts the local symmetry of the ion. This symmetry reduction splits the triply orbital degeneracy of the ${}^7\text{F}_1$ state into three non-degenerate A + E states. Such a change in point symmetry must increase the probability of radiative transitions of the Eu^{3+} excited state. This is consistent with the results shown in Table S7 (ESI†).

It is important to note that the interpretation of CF parameter variations requires a detailed analysis of the crystal structure and electronic properties of the material. Theoretical simulations and additional experiments may be required to unveil the underlying mechanisms and establish a precise correlation between Bi^{3+} concentration, CF parameters, and the luminescent properties of the material.

Temperature sensing

Since the PL peaks of the ${}^5\text{D}_{0,1}$ levels for Eu^{3+} and the ${}^2\text{F}_{5/2}$ transition for Yb^{3+} are the most intense in NYMO:0.05 Eu^{3+} / $y\text{Bi}^{3+}$, it was the sample of choice for thermometric measurements. Its temperature dependent PL spectra are presented in Fig. 5. The temperature was varied over a wide range from 298 to 525 K. It can be seen that temperature affects the intensity of the different emission bands in a different way. Specifically, the intensities of the photoluminescence (PL) bands peaking at 534, 589, 614, 702 and 993 nm all decrease significantly with increasing temperature over the entire temperature range studied. This decrease in PL intensity at relatively high temperatures can be attributed to a thermal extinction phenomenon.⁵⁶ This phenomenon is linked to an increase in the probability of non-radiative transitions between the excited energy levels of the Eu^{3+} ion and the crystal lattice as temperature increases.

Further analysis of the emission spectra reveals an interesting relationship between the FIR (integrated fluorescence ratio) value of the areas under the emission bands at 589 and 614 nm and temperature. These two emission bands correspond to the ${}^5\text{D}_0 \rightarrow {}^7\text{F}_1$ (MD) and ${}^5\text{D}_0 \rightarrow {}^7\text{F}_2$ (ED) transitions of the Eu^{3+} ion, respectively. The ground state ${}^7\text{F}_0$ is excited to the ${}^5\text{L}_6$ level and subsequently relaxes non-radiatively to the lower energy state ${}^5\text{D}_0$. Radiative transitions then occur to the ${}^7\text{F}_1$ and ${}^7\text{F}_2$ levels, resulting in red emission. The FIR can be expressed as the ratio of the emission intensity of ${}^5\text{D}_0 \rightarrow {}^7\text{F}_1$ to that of ${}^5\text{D}_0 \rightarrow {}^7\text{F}_2$. According to the Boltzmann distribution, the populations of these energy levels follow an inverse exponential distribution with temperature^{57,58}:

$$\text{FIR} = A \times \exp\left(\frac{-\Delta E}{KT}\right) \quad (3)$$



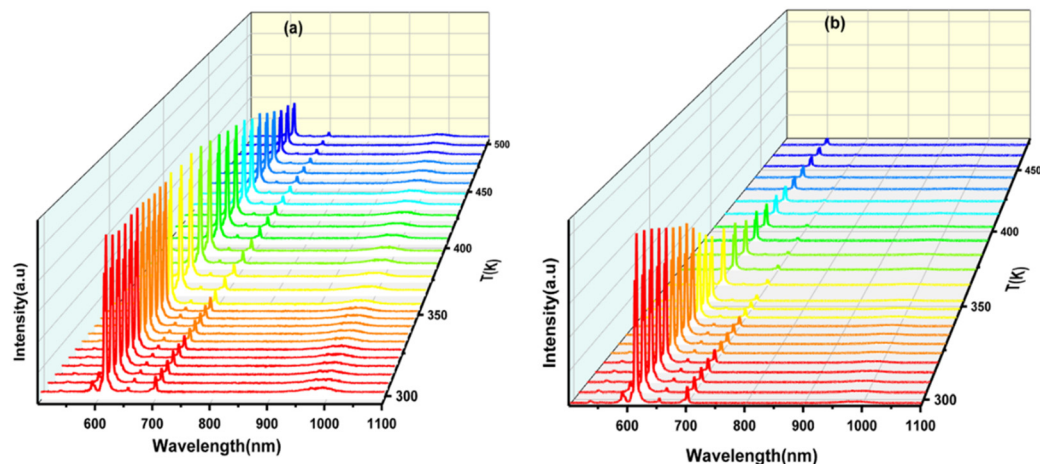


Fig. 5 Temperature-dependent PL of the NYMO phosphor (a) doped 0.05Eu³⁺ and (b) codoped 0.05Eu³⁺/0.05Bi³⁺ excited at 325 nm.

where A is a constant pre-exponential factor. ΔE is the energy difference between the $^5D_0 \rightarrow ^7F_2$ and $^5D_0 \rightarrow ^7F_1$ transitions. k is Boltzmann's constant ($k = 8617 \times 10^{-5} \text{ eV K}^{-1}$).

Furthermore, as the temperature increases from 298 K to 523 K, an increase in the FIR ratio is observed, and this increase could be attributed to lattice expansion during heating. The FIR

ratio is sensitive to the covalent nature of the $\text{Eu}^{3+} \rightarrow \text{O}^{2-}$ bond and the asymmetric nature of the Eu^{3+} site. Lattice expansion upon heating increases the bond distance of the $\text{Eu}^{3+} \rightarrow \text{O}^{2-}$ bond, leading to an increase in covalency and consequently an increase in FIR.⁵⁹ Also, this confirms that the populations of the 7F_1 and 7F_2 energy levels follow a Boltzmann distribution,

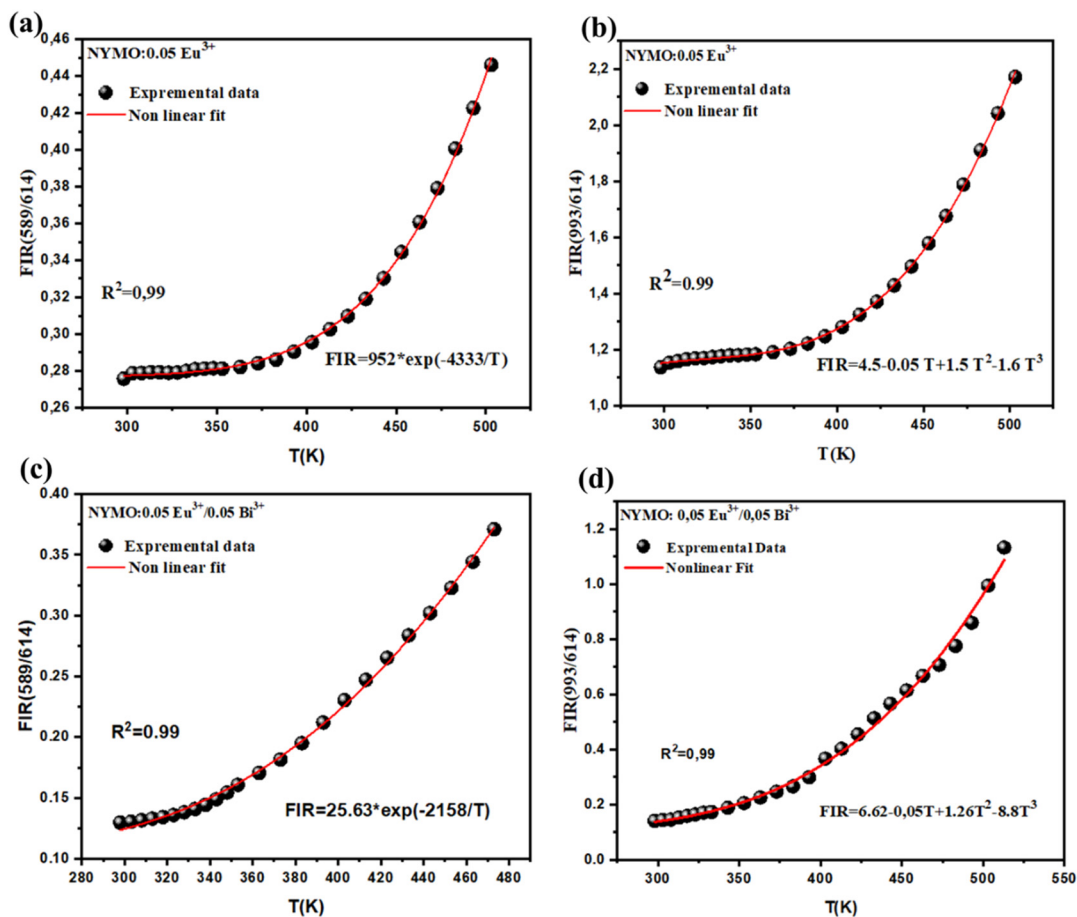


Fig. 6 FIR vs. temperature variations for NYMO:0.05Eu³⁺ and NYMO:0.05Eu³⁺/0.05Bi³⁺.



and that thermal extinction is the primary mechanism responsible for the decrease in PL intensity at high temperatures. The FIR is correctly fitted and plotted as a function of temperature in Fig. 6.

The emission intensity ratio of Yb^{3+} (993 nm) and Eu^{3+} (614 nm) ions, defined as FIR (993/614), is adopted to study the temperature-dependent photoluminescence property. The FIR (I_{Yb}/I_{Eu}) can be fitted as:^{60,61}

$$\text{FIR} = A + B \times T + C \times T^2 + D \times T^3 \quad (4)$$

Absolute sensitivity (S_a) and relative sensitivity (S_r) are two key factors in assessing the performance of optical thermometry. S_a and S_r are defined respectively as the rate of change and the relative rate of change of the FIR as a function of temperature, which can be calculated according to the following equations:⁶²

$$S_a = \left| \frac{\partial \text{FIR}}{\partial T} \right| \quad (5)$$

$$S_r = \frac{1}{\text{FIR}} \left| \frac{\partial \text{FIR}}{\partial T} \right| \quad (6)$$

The value of S_a for the FIR (589/614) ratio, at a maximum at 0.0016 K⁻¹, increases monotonically with temperature, while

that of S_r , at a maximum at 0.68 K⁻¹, exhibits an approximate parabolic variation with temperature. S_r and S_a reach a maximum at 495 K. For uncoupled levels, we observe an increase in S_a , peaking at 0.0014 K⁻¹. While S_r has a maximum at 0.7 K⁻¹ which shows an approximately parabolic variation with temperature, as shown in Fig. 7. Furthermore, for NYMO:0.05Eu³⁺/0.05Bi³⁺, the sensitivities for the FIR ratio increase with increasing temperature. The S_r sensitivity peaks at 495 K, at approximately 0.72% K⁻¹. High Ω_2 , as estimated here, occurs in the case of a high covalence of the Eu–O bond for an optimal concentration of 5% Bi³⁺. S_a is directly related to the Judd–Ofelt parameter, and this value has the same variation as that of Ω_2 .⁶³ With the addition of bismuth, there is an increase in the thermometric values (S_r), by relating it to ΔE , which express the energy of the intersection point between the ground and excited state parabolas, which can be directly determined based on the emission intensity measurement vs temperature. In the case of the analyzed phosphors, ΔE decreases as follows: 2761.29 cm⁻¹ and 2022.93 cm⁻¹ for NYMO:0.05Eu³⁺ and NYMO:0.05Eu³⁺/0.05Bi³⁺ respectively.

However, for the FIR ratio (993/614), the sensitivities increase up to 350 K ($S_{r\text{max}} = 1.14\% \text{ K}^{-1}$). After this temperature

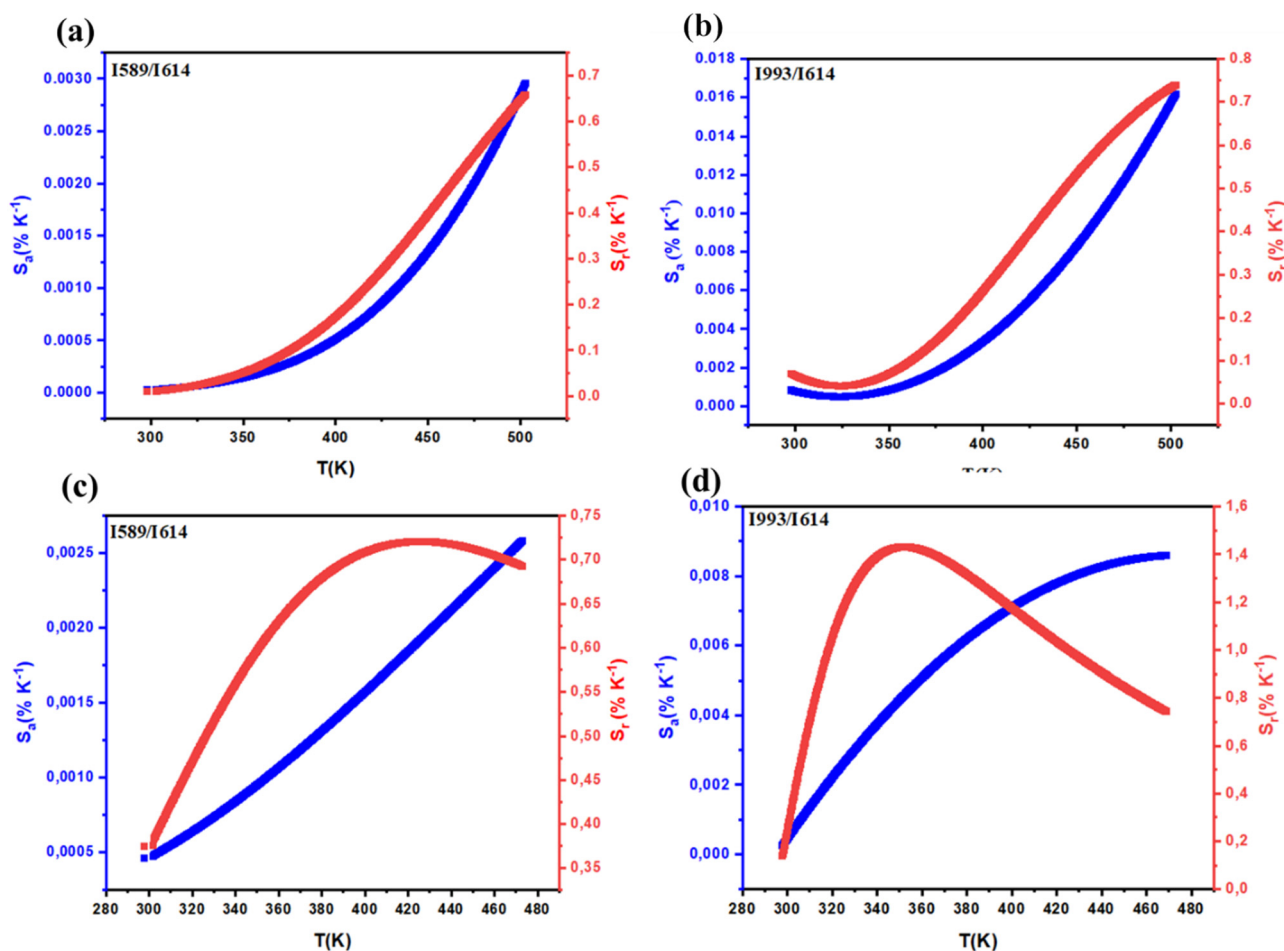


Fig. 7 S_a absolute and S_r relative sensitivity variations with temperature of NYMO:0.05Eu³⁺ (a) and (b) and NYMO:0.05Eu³⁺/0.05Bi³⁺ (c) and (d) under 325 nm excitation.



Table 1 Sensitivities and temperature range for the temperature-sensing luminescence materials

Materials	Temperature range (K)	S_{amax} (K^{-1})	S_{rmax} (K^{-1})	Ref.
$\text{SrLu}_2\text{O}_7:\text{Eu}^{3+}/\text{Bi}^{3+}$	313–543	0.011	0.87	66
$\text{Ca}_2\text{Y}_8(\text{SiO}_4)_6\text{O}_2:\text{Eu}^{3+}/\text{Bi}^{3+}$	298–523	0.0717	0.96	67
$\text{NaCaPO}_4:\text{Tb}^{3+}/\text{Eu}^{3+}$	293–573	—	0.66	68
$\text{Ba}_2\text{TiGe}_2\text{O}_8:\text{Eu}^{3+}$	358–548	—	0.93	69
$\text{La}_2\text{LiNbO}_6:\text{Eu}^{3+}/\text{Bi}^{3+}$	298–498	0.0247	0.9	70
$\text{Gd}_2\text{Zr}_2\text{O}_7:\text{Eu}^{3+}$	300–700	—	0.92	71
NaEuF_4	395	—	0.24	72
$\text{Gd}_2\text{Ti}_2\text{O}_7:\text{Eu}^{3+}$	303–423	0.015	0.95	73
$\text{Ca}_8\text{ZnLa}(\text{PO}_4)_7:\text{Tb}^{3+}/\text{Eu}^{3+}$	298–448	0.0025	0.53	74
$\text{KBaGd}(\text{WO}_4)_3:\text{Dy}^{3+}/\text{Eu}^{3+}$	298–478	0.033	0.64	75
$\text{NaYb}(\text{MoO}_4)_2:\text{Eu}^{3+}/\text{Bi}^{3+}$	298–503	0.002	1.14	This work

the S_r decreases. When examining the absolute and relative sensitivity trends between NYMO doped with 0.05Eu^{3+} and NYMO doped with $0.05\text{Eu}^{3+}/0.05\text{Bi}^{3+}$, we observe a clear S_r and S_a value increase with the addition of bismuth. As a result, NYMO codoped with Eu^{3+} and Bi^{3+} seems highly suitable for temperature sensing applications.

Thermal resolution is determined by the actual temperature measured by the sensor and the precision of the experimental detection device, as shown below:^{64,65}

$$\delta T = \frac{1}{S_R} \frac{\delta \text{FIR}}{\text{FIR}} \quad (7)$$

where $\delta \text{FIR}/\text{FIR}$ is estimated from the integrated area of the transitions.

FIR uncertainty (δFIR) was determined as the standard deviation of the statistical distribution for each method. Using eqn (7), it is clear that these values are less than 0.5 K for FIR (589/613) and 0.25 K for FIR (993/613), indicating high accuracy for both FIR techniques over the entire temperature range studied. Fig. S5 (ESI[†]) shows the calculated values of temperature resolution. Note that the δT value shows a decreasing trend with increasing Bi^{3+} concentrations and all δT values are below 0.35 K for FIR (589/613) and 0.12 K for FIR (993/613), indicating that the designed phosphors have excellent temperature resolution.

Table 1 evidences a sensitivity of our samples higher than the previously reported values in other host materials. From the comparative analysis presented in Table 1, it is evident that the $\text{NaYb}(\text{MoO}_4)_2:\text{Eu}^{3+}/\text{Bi}^{3+}$ phosphor synthesized in this work shows unique thermometric properties within the temperature range of 298–503 K. Specifically, although its maximum absolute sensitivity (S_{amax}) of 0.002 K^{-1} is lower than that of other materials, such as $\text{Ca}_2\text{Y}_8(\text{SiO}_4)_6\text{O}_2:\text{Eu}^{3+}/\text{Bi}^{3+}$ (0.0717 K^{-1}) and $\text{KBaGd}(\text{WO}_4)_3:\text{Eu}^{3+}$ (0.033 K^{-1}), it exhibits an exceptionally high relative sensitivity (S_{rmax}) of 1.14 K^{-1} . This S_{rmax} value surpasses that of all other materials in the comparison, making it particularly promising for applications requiring high temperature resolution and accuracy. The combination of moderate temperature range, improved relative sensitivity, and stable luminescence intensity positions NYMO:0.05 $\text{Eu}^{3+}/0.05\text{Bi}^{3+}$ as a competitive candidate for advanced optical thermometry applications, where high precision is critical.

Conclusion

A series of Eu^{3+} -activated NYMO phosphors co-doped with Bi^{3+} were synthesized *via* solid-state reaction, confirming a tetragonal crystal structure. Under UV excitation, strong emissions from Eu^{3+} (589, 613, 652, 700 nm) and Yb^{3+} (997 nm), sensitized by MoO_4^{2-} , were observed. The introduction of Bi^{3+} not only increased the energy gap ($\sim 3.25 \text{ eV}$ for 5% Bi^{3+}) but also significantly enhanced the luminescence emission, particularly, the red emissions from Eu^{3+} . Chromaticity analysis revealed a shift in CIE coordinates with increasing Bi^{3+} content, confirming intensified red emission and improved color purity, with the highest purity (87.21%) observed at 5% Bi^{3+} . Additionally, Judd–Ofelt parameters showed that the introduction of Bi^{3+} affects the electric-dipole transitions of Eu^{3+} ions, with the Ω_2 parameter increasing for low Bi^{3+} concentrations (up to 0.05) before stabilizing, while Ω_4 decreased with increasing Bi^{3+} , suggesting that moderate doping optimizes luminescence. The calculated crystal field parameters demonstrated that moderate Bi^{3+} doping, especially at 5%, optimizes the crystal field strength, enhancing the luminescence performance. However, higher concentrations (20%) lead to significant alterations of the crystal field, potentially affecting luminescence negatively. Furthermore, the incorporation of Bi^{3+} also improved the material's optical thermometry performance by increasing Eu^{3+} emission and temperature sensitivity, with a maximum absolute sensitivity (S_{amax}) of 0.002 K^{-1} and a notable relative sensitivity (S_{rmax}) of 1.14 K^{-1} , enabling superior temperature resolution. In summary, Bi^{3+} doping significantly enhances the optical, structural, chromatic, and thermometric properties of the phosphors, making them highly suitable for advanced optoelectronic devices and temperature sensing applications.

Data availability

All data underlying the results are available as part of the article and no additional source data are required.

Conflicts of interest

There are no conflicts to declare.



Acknowledgements

Mediavilla, and J. Jimenez were partly funded by the Spanish Ministry of Science and Innovation (Grants PID2021-126046OB-C22, PID2020-113533RB-C33, TED2021-130786B-I00), and the Regional Government of Castilla y León (Junta de Castilla y León) and by the Ministry of Science and Innovation and the European Union NextGenerationEU/PRTR under the project 'Programa Complementario de Materiales Avanzados'. I. Kchaou was funded by the Erasmus+ KA171 Project.

References

- 1 M. G. Brik and A. M. Srivastava, *Luminescent Materials: Fundamentals and Applications*, De Gruyter, Berlin, Germany; Boston, MA, USA, 2023.
- 2 L. D. Carlos and F. Palacio, *Thermometry at the Nanoscale: Techniques and Selected Applications*, Royal Society of Chemistry, Cambridge, CA, USA, 2016.
- 3 M. Quintanilla and L. M. Liz-Marzán, Guiding Rules for Selecting a Nanothermometer, *Nano Today*, 2018, **19**, 126–145.
- 4 C. Bradac, S. F. Lim, H.-C. Chang and I. Aharonovich, Optical Nanoscale Thermometry: From Fundamental Mechanisms to Emerging Practical Applications, *Adv. Opt. Mater.*, 2020, **8**, 2000183.
- 5 A. Nexha, J. J. Carvajal, M. C. Pujol, F. Díaz and M. Aguiló, Lanthanide doped luminescence nanothermometers in the biological windows: Strategies and applications, *Nanoscale*, 2021, **13**, 7913.
- 6 F. Liao, B. Shen, W. Wu, Y. Zhang and J. Hu, A Study on the Anti-Thermal $\text{Dy}^{3+}/\text{Eu}^{3+}$ Co-Doped $\text{BaLa}_4\text{Si}_3\text{O}_{13}$ Red Phosphors for White-Light-Emitting Diodes and Optical Thermometry Applications, *Ind. Eng. Chem. Res.*, 2021, **60**(7), 2931–2943.
- 7 M. Back, J. Ueda, H. Nambu, M. Fujita, A. Yamamoto, H. Yoshida, H. Tanaka, M. Brik and S. Tanabe, Boltzmann thermometry in Cr^{3+} -doped Ga_2O_3 polymorphs: the structure matters!, *Adv. Opt. Mater.*, 2021, **9**, 2100033.
- 8 J. Stefanska, A. Bednarkiewicz and L. Marciniak, Advancements in excited state absorption-based luminescence thermometry, *J. Mater. Chem. C*, 2022, **10**, 5744–5782.
- 9 K. Wang, Y. Liu, D. Liu, G. Tan, S. Bai and H. Ren, *et al.*, Enhancing Sm^{3+} emission of $\text{LiLa}(\text{MoO}_4)_2:\text{Sm}^{3+}$, Bi^{3+} phosphors by non-sensitization of Bi^{3+} , *J. Lumin.*, 2019, **214**, 116590.
- 10 P. Du, X. Huang and J. Yu, Yb^{3+} -Concentration dependent upconversion luminescence and temperature sensing behavior in $\text{Yb}^{3+}/\text{Er}^{3+}$ codoped Gd_2MoO_6 nanocrystals prepared by a facile citric-assisted sol-gel method, *Inorg. Chem. Front.*, 2017, **4**, 1987–1995.
- 11 L. Daćanin Far and M. D. Dramićanin, Luminescence Thermometry with Nanoparticles: Luminescence Thermometry with Nanoparticles: A Review, *Nanomaterials*, 2023, **13**, 2904.
- 12 A. Zhang, Z. Sun, G. Liu, Z. Fu, Z. Hao, J. Zhang and Y. Wei, Ln^{3+} (Er^{3+} , Tm^{3+} and Ho^{3+})-Doped $\text{NaYb}(\text{MoO}_4)_2$ Upconversion Phosphors as Wide Range Temperature Sensors with High Sensitivity, *J. Alloys Compd.*, 2017, **728**, 476–483.
- 13 P. Du, X. Huang and J. S. Yu, Facile Synthesis of Bifunctional Eu^{3+} -Activated NaBiF_4 Red-Emitting Nanoparticles for Simultaneous White Light-Emitting Diodes and Field Emission Displays, *Chem. Eng. J.*, 2018, **337**, 91–100.
- 14 T. Sakthivel, G. Annadurai, R. Vijayakumar and X. Huang, Synthesis, Luminescence Properties and Thermal Stability of Eu^{3+} -Activated $\text{Na}_2\text{Y}_2\text{B}_2\text{O}_7$ Red Phosphors Excited by near-UV Light for Pc-WLEDs, *J. Lumin.*, 2019, **205**, 129–135.
- 15 B. Z. Yang, Z. P. Yang and Y. F. Liu, *et al.*, *Ceram. Int.*, 2012, **38**, 4895–4900.
- 16 A. Yousif and H. C. Swart, Colour tuneable emission from $(\text{Y}_{1.995-x}\text{Ga}_x)_2\text{O}_3:\text{Bi}^{3+}$ phosphor prepared by a sol-gel combustion method, *Mater. Lett.*, 2017, **186**, 345–348.
- 17 Bismuth- and erbium-doped optical fiber with ultrabroad-band luminescence and high optical gain.
- 18 K. Saidi, I. Kachou, K. S. Carracedo, M. Dammak and I. R. Martín, $\text{Ba}_2\text{YV}_3\text{O}_{11}:\text{Er}^{3+}/\text{Yb}^{3+}$ Nanostructures for Temperature Sensing in the Presence of Bismuth Ions, 2023, DOI: [10.1021/acsanm.3c02911](https://doi.org/10.1021/acsanm.3c02911).
- 19 K. Saidi, C. Hernández-Álvarez, M. Runowski, M. Dammak and I. R. Martín, *Dalton Trans.*, 2023, **52**, 14904–14916.
- 20 I. Kachou, K. Saidi, R. Salhi and M. Dammak, Synthèse et Optique Spectroscopie de $\text{N/A}_3\text{Y}(\text{VO}_4)_2:\text{UE}^{3+}$ Phosphores pour Applications de thermométrie et d'affichage, *RSC Adv.*, 2022, **12**(12), 7529–7539.
- 21 G. Li, L. Li, M. Li, W. Bao, Y. Song, S. Gan, H. Zou and X. Xu, *J. Alloys Compd.*, 2013, **550**, 1–8.
- 22 Y. Wang, C. Lin, H. Zheng, D. Sun, L. Li and B. Chen, *J. Alloys Compd.*, 2013, **559**, 123–128.
- 23 S.-F. Wang, K. Koteswara Rao, Y.-R. Wang, Y.-F. Hsu, S.-H. Chen and Y.-C. Lu, *J. Am. Ceram. Soc.*, 2009, **92**, 1732–1738.
- 24 L. Xu, X. Yang, H. Lu, C. Hu and W. Hou, $\text{NaY}(\text{MoO}_4)_2$ microcrystals with controlled faceting and their tunable photoluminescence properties after doping with Eu^{3+} , *RSC Adv.*, 2014, **4**(26), 13502–13508.
- 25 B. Yan and J.-H. Wu, $\text{NaY}(\text{MoO}_4)_2:\text{Eu}^{3+}$ and $\text{NaY}_{0.9}\text{Bi}_{0.1}(\text{MoO}_4)_2:\text{Eu}^{3+}$ submicrometer phosphors: Hydrothermal synthesis assisted by room temperature-solid state reaction, microstructure and photoluminescence, *Mater. Chem. Phys.*, 2009, **116**(1), 67–71, DOI: [10.1016/j.matchemphys.2009.02.042](https://doi.org/10.1016/j.matchemphys.2009.02.042).
- 26 S. Yan, J. Zhang, X. Zhang, S. Lu, X. Ren, Z. Nie and X. Wang, Enhanced Red Emission in $\text{CaMoO}_4:\text{Bi}^{3+}, \text{Eu}^{3+}$, *J. Phys. Chem. C*, 2007, **111**, 13256–13260.
- 27 Correction to: White-light/tunable emissions in single-phased $\text{BaLa}_2\text{Si}_3\text{O}_{10}:\text{Eu}^{3+}, \text{Bi}^{3+}$ phosphor for the simultaneous applications in white light-emitting diodes and luminous cement – ProQuest.
- 28 A. Ćirić, S. Stojadinović and M. D. Dramićanin, An extension of the Judd-Ofelt theory to the field of lanthanide thermometry, *J. Lumin.*, 2019, **216**, 116749.



- 29 A. Zhang, M. Jia, Z. Sun, G. Liu, Z. Fu, T. Sheng, P. Li and F. Lin, High concentration Eu^{3+} -doped $\text{NaYb}(\text{MoO}_4)_2$ multi-functional material: Thermometer and plant growth lamp matching phytochrome PR, *J. Alloys Compd.*, 2019, **782**, 203–208.
- 30 R. D. Shannon, Revised effective ionic radii and systematic studies of interatomic distances in halides and chalcogenides, *Acta Crystallogr., Sect. A*, 1976, 751–767.
- 31 J. Liao, P. Xie, W. Li, Z. Chen, Z. Liu and L. Chen, *et al.*, White-light/tunable emissions in single-phased $\text{BaLa}_2\text{Si}_3\text{O}_{10}:\text{Eu}^{3+}$, Bi^{3+} phosphor for the simultaneous applications in white light-emitting diodes and luminous cement, *J. Mater. Sci.: Mater. Electron.*, 2019, **31**, 1–10.
- 32 J. Zhang, Y. Liu, L. Li, N. Zhang, L. Zou and S. Gan, Hydrothermal synthesis, characterization, and color-tunable luminescence properties of $\text{Bi}_2\text{MoO}_6:\text{Eu}^{3+}$ phosphors, *RSC Adv.*, 2015, 5(37), 29346–29352.
- 33 H. Ji, L. Wang, M. S. Molokeev, N. Hirotsaki, R. Xie and Z. Huang, *et al.*, Structure evolution and photoluminescence of $\text{Lu}_3(\text{Al}, \text{Mg})_2(\text{Al}, \text{Si})_3\text{O}_{12}:\text{Ce}^{3+}$ phosphors: new yellow-color converters for blue LED-driven solid state lighting, *J. Mater. Chem. C*, 2016, 4(28), 6855–6863.
- 34 W. T. Zhang, J. F. Li, Y. L. Wang, J. P. Long and K. H. Qiu, Synthesis and luminescence properties of $\text{NaLa}(\text{MoO}_4)_{2-x}\text{AG}_x:\text{Eu}^{3+}$ ($\text{AG} = \text{SO}_4^{2-}$, BO_3^{2-}) red phosphors for white light emitting diodes, *J. Alloys Compd.*, 2015, **635**, 16–20.
- 35 B. Devakumar, P. Halappa and C. Shivakumara, $\text{Dy}^{3+}/\text{Eu}^{3+}$ co-doped $\text{CsGd}(\text{MoO}_4)_2$ phosphor with tunable photoluminescence properties for near-UV WLEDs applications, *Dyes Pigm.*, 2017, **137**, 244–255.
- 36 S. Tomar and C. Shivakumara, Enhanced Emission Intensity in $(\text{Li}^+/\text{Ca}^{2+}/\text{Bi}^{3+})$ Ions Co-doped $\text{NaLa}(\text{MoO}_4)_2:\text{Dy}^{3+}$ phosphors and Their Judd–Ofelt Analysis for WLEDs Applications, *Methods Appl. Fluoresc.*, 2023, **11**, 024001.
- 37 G. Annadurai, B. Li, B. Devakumar, H. Guo, L. Sun and X. Huang, *J. Lumin.*, 2019, **208**, 75–81.
- 38 T. Liu, Q. Y. Meng and W. J. Sun, Electron-phonon coupling properties and energy transfer in $\text{NaY}(\text{WO}_4)_2:\text{Eu}^{3+}$ phosphor, *J. Alloys Compd.*, 2015, **647**, 830.
- 39 F. W. Kang, Y. Zhang and M. Peng, Controlling the Energy Transfer via Multi Luminescent Centers to Achieve White Light/Tunable Emissions in a Single-Phased X_2 -Type $\text{Y}_2\text{SiO}_5:\text{Eu}^{3+}, \text{Bi}^{3+}$ Phosphor For Ultraviolet Converted LEDs, *Inorg. Chem.*, 2015, **54**, 1462–1473.
- 40 J. Huang, Z. W. Yang, C. Y. Yu, Z. Z. Chai, J. B. Qiu and Z. G. Song, Tunable and White Light Emission of a Single-Phased $\text{Ba}_2\text{Y}(\text{BO}_3)_2\text{Cl}:\text{Bi}^{3+}, \text{Eu}^{3+}$ Phosphor by Energy Transfer for Ultraviolet Converted White LEDs, *J. Phys. Chem. C*, 2017, **121**, 5267–5276.
- 41 R. Lu, X. Zhang, Y. Fang, X. Wu, M. Jia, K. Wang, J. Wu, Q. Li and Z. Sun, Europium Ions Self-Reduction Benefiting from $\text{AlO}_4/\text{Si}(\text{Al})\text{O}_4$ Network Structure for Multimode Optical Thermometry Manometry, *Laser Photonics Rev.*, 2024, 2400409.
- 42 S. Tomar and C. Shivakumara, Enhanced Emission Intensity in $(\text{Li}^+/\text{Ca}^{2+}/\text{Bi}^{3+})$ Ions Co-Doped $\text{NaLa}(\text{MoO}_4)_2:\text{Dy}^{3+}$ phosphors and Their Judd–Ofelt Analysis for WLEDs Applications, *Methods Appl. Fluoresc.*, 2023, **11**, 024001.
- 43 S. Cui, W. Xu, Y. Zhu, X. Chen, D. Zhou, Z. Yin, H. Song and W. Han, Highly modified spontaneous emission in $\text{NaY}(\text{MoO}_4)_2:\text{Yb}^{3+}/\text{Er}^{3+}$ inverse opal photonic crystals, *RSC Adv.*, 2015, 5, 104862–104869.
- 44 P. Singh, S. Modanwal, H. Mishra and S. B. Rai, Intense Photoluminescence in $\text{CaTiO}_3:\text{Sm}^{3+}$ Phosphors, Effect of Co-Doping Singly, Doubly and Triply Ionized Elements and Their Applications in LEDs, *RSC Adv.*, 2023, **13**, 22663–22674.
- 45 C. S. McCamy, Correlated Color Temperature as an Explicit Function of Chromaticity Coordinates, *Color Res. Appl.*, 1992, 17, 142–144.
- 46 P. Singh, S. Modanwal, H. Mishra and S. B. Rai, Intense Photoluminescence in $\text{CaTiO}_3:\text{Sm}^{3+}$ Phosphors, Effect of Co-Doping Singly, Doubly and Triply Ionized Elements and Their Applications in LEDs, *RSC Adv.*, 2023, **13**, 22663–22674.
- 47 N. Dhananjaya, C. Shivakumara, R. Saraf and H. Nagabhushana, Red-emitting $\text{LaOF}:\text{Eu}^{3+}$ phosphors: Synthesis, structure and their Judd–Ofelt analysis for LED applications, *Mater. Res. Bull.*, 2016, 75, 100–109.
- 48 F. Lei and B. Yan, Hydrothermal synthesis and luminescence of $\text{CaMO}_4:\text{RE}^{3+}$ ($\text{M} = \text{W}, \text{Mo}$; $\text{RE} = \text{Eu}, \text{Tb}$) submicro-phosphors, *J. Solid State Chem.*, 2008, **181**(4), 855–862.
- 49 H. George, N. Deopa, S. Kaur, A. Prasad, M. Sreenivasulu and M. Jayasimhadri, *et al.*, Judd–Ofelt parametrization and radiative analysis of Dy^{3+} ions doped Sodium Bismuth Strontium Phosphate glasses, *J. Lumin.*, 2019, **215**, 116693.
- 50 A. Ćirić, S. Stojadinović, M. Sekulić and M. D. Dramićanin, JOES: an application software for Judd–Ofelt analysis from Eu^{3+} emission spectra, *J. Lumin.*, 2018, S0022-2313(18)31329-2.
- 51 Thermal, optical and spectroscopic assessment of $\text{Yb}^{3+}:\text{NaY}(\text{MoO}_4)_2$ single crystal as a potential diode pumped laser near 1.04 μm , *Solid State Commun.*, 2008.
- 52 S. G. Prasanna Kumar, R. Hari Krishna, N. Kottam, P. Krishna Murthy, C. Manjunatha and R. Preetham, *et al.*, Understanding the photoluminescence behaviour in nano $\text{CaZrO}_3:\text{Eu}^{3+}$ pigments by Judd–Ofelt intensity parameters, *Dyes Pigm.*, 2018, **2018**(150), 306–314.
- 53 M. Dolores, C. Cascales, X. Han, C. Zaldo, A. Jezowski, P. Stachowiak, N. Ter-Gabrielyan, V. Fromzel and M. Dubinskii, Thermal Characterization, Crystal Field Analysis and In Band Pumped Laser Performance of Er Doped $\text{NaY}(\text{WO}_4)_2$ Disordered Laser Crystals, *PLoS One*, 2013, 29255-C02-01.
- 54 M. Karbowiak, E. Zych and J. H. Is, *J. Phys.: Condens. Matter*, 2003, **15**, 2169.
- 55 *Energy levels, fluorescence lifetime and Judd–Ofelt parameters of Eu^{3+} in Gd_2O_3 nanocrystals*, IOP Science.
- 56 W. Yu, W. Xu, H. Song and S. Zhang, Temperature-dependent upconversion luminescence and dynamics of $\text{NaYF}_4:\text{Yb}^{3+}/\text{Er}^{3+}$ nanocrystals: influence of particle size and crystalline phase, *Dalton Trans.*, 2014, **43**(16), 6139–6147.



- 57 Z. E. A. A. Taleb, K. Saïdi, M. Dammak, D. Przybylska and T. Grzyb, Thermométrie optique ultrasensible utilisant Tb³⁺ NaSrGd-dopé(Meuglement₄)₃ Basé sur la luminescence ratiométrique à bande unique, *Dalton Trans.*, 2023, **52**, 4954–4963.
- 58 M. Runowski, S. Goderski, D. Przybylska, T. Grzyb, S. Lis and I. R. Martin, Sr₂LuF₇:Yb³⁺–Ho³⁺–Eu³⁺ Conversion ascendante Les nanoparticules comme thermomètres luminescents dans les premier, deuxième et troisième cycles et la troisième fenêtre biologique, *ACS Appl. Nano Mater.*, 2020, **3**(7), 6406–6415.
- 59 J. Cheng, J. Zhang, X. Bian, Z. Zhai and J. Shi, Photoluminescence properties, JuddOfelt analysis, and optical temperature sensing of Eu³⁺-doped Ca₃La₇(SiO₄)₅(PO₄) O₂ luminescent materials, *Spectrochim. Acta, Part A*, 2020, **230**, 118057.
- 60 N. Kumar Mishra, M. M. Upadhyay, S. Kumar and K. Kumar, Efficient Dual Mode Emission in Ce³⁺/Yb³⁺/Er³⁺ Doped Yttrium Aluminium Gallium Garnet for Led Device and Optical Thermometry, *Spectrochim. Acta, Part A*, 2022, **282**, 12166.
- 61 W. Xu, X. Y. Gao, L. J. Zheng, Z. G. Zhang and W. W. Cao, An optical temperature sensor based on the upconversion luminescence from Tm³⁺/Yb³⁺ co-doped oxyfluoride glass ceramic, *Sens. Actuators, B*, 2012, **173**, 250–253.
- 62 Y. Luo, L. Zhang, Y. Liu, E. Heydari, L. Chen and G. Bai, Designing Dual-Mode Luminescence in Er³⁺ Doped Y₂WO₆ Micro? particles for Anticounterfeiting and Temperature Measurement, *J. Am. Ceram. Soc.*, 2022, **105**, 1375–1385.
- 63 A. V. Egorysheva, V. D. Volodin, A. A. Chistyakov, Y. A. Kuzishchin, V. M. Skorikov and T. D. Dudkina, Luminescence of europium-doped BaO–Bi₂O₃–B₂O₃ glasses, *Inorg. Mater.*, 2010, **46**, 1384–1390.
- 64 F. Ayachi, K. Saidi, W. Chaabani and M. Dammak, Synthesis and Luminescence Properties of Er³⁺ Doped and Er³⁺–Yb³⁺ Codoped Phosphovanadate YP_{0.5}V_{0.5}O₄ Phosphors, *J. Lumin.*, 2021, **240**, 118451.
- 65 K. Saidi, M. Dammak, K. Soler-Carracedo and I. R. Martín, A Novel Optical Thermometry Strategy Based on Emission of Tm³⁺/Yb³⁺ Codoped Na₃GdV₂O₈ Phosphors, *Dalton Trans.*, 2022, **51**(13), 5108–5117.
- 66 X. Chen, Z. Zheng, L. Teng, R. Wei, F. Hu and H. Guo, Self-calibrated optical thermometer based on luminescence from SrLu₂O₄:Bi³⁺,Eu³⁺ phosphors, *RSC Adv.*, 2018, **8**, 35422–35428.
- 67 K. Li and R. Van Deun, Site-Bi³⁺ and Eu³⁺ dual emissions in color-tunable Ca₂Y₈(SiO₄)₆O₂:Bi³⁺,Eu³⁺ phosphors prepared via sol-gel synthesis for potentially ratiometric temperature sensing, *J. Alloys Compd.*, 2019, **787**, 86–95.
- 68 L.-Q. Yao, G.-H. Chen, T. Yang, S.-C. Cui, Z.-C. Li and Y. Yang, Energy Transfer, Tunable Emission and Optical Thermometry in Tb³⁺/Eu³⁺ Co-Doped Transparent NaCaPO₄ Glass Ceramics, *Ceram. Int.*, 2016, **42**(11), 13086–13090.
- 69 B. Hou, M. Jia, P. Li, G. Liu, Z. Sun and Z. Fu, Multi-functional Optical Thermometry Based on the Rare-Earth-Ions Doped Up-/Down-Conversion Ba₂TiGe₂O₈:Ln (Ln = Eu³⁺/Er³⁺/Ho³⁺/Yb³⁺) Phosphors, *Inorg. Chem.*, 2019, **58**, 7939–7946.
- 70 M. Song, W. Ran, Y. Ren, L. Wang and W. Zhao, Characterizations and photoluminescence properties of a dual-functional La₂LiNbO₆:Bi³⁺,Eu³⁺ phosphor for WLEDs and ratiometric temperature sensing, *J. Alloys Compd.*, 2021, **865**, 158825.
- 71 A. Kumar and J. Manam, Color tunable emission and temperature dependent photoluminescence properties of Eu³⁺ co-doped Gd₂Zr₂O₇:Dy³⁺ phosphors, *Opt. Mater.*, 2019, **96**, 109373.
- 72 Y. Tian, B. Tian, C. Cui, P. Huang, L. Wang and B. Chen, Excellent optical thermometry based on single-color fluorescence in spherical NaEuF₄ phosphor, *Opt. Lett.*, 2014, **39**(14), 4164–4167.
- 73 V. Lojpur, S. Čulubrk and M. D. Dramićanin, Ratiometric luminescence thermometry with different combinations of emissions from Eu³⁺ doped Gd₂Ti₂O₇ nanoparticles, *J. Lumin.*, 2016, **169**, 534–538, DOI: [10.1016/j.jlumin.2015.01.027](https://doi.org/10.1016/j.jlumin.2015.01.027).
- 74 L. Li, X. Tang, Z. Wu, Y. Zheng, S. Jiang, X. Tang, G. Xiang and X. Zhou, Simultaneously tuning emission color and realizing optical thermometry via efficient Tb³⁺ → Eu³⁺ energy transfer in whitlockite-type phosphate multifunctional phosphors, *J. Alloys Compd.*, 2019, **780**, 266–275.
- 75 D. Huang, P. Dang, H. Lian, Q. Zeng and J. Lin, Luminescence and energy-transfer properties in Bi³⁺/Mn⁴⁺-codoped Ba₂GdNbO₆ double-perovskite phosphors for white-light-emitting diodes, *Inorg. Chem.*, 2019, **58**, 15507–15519.

